Title
Imaging and Modeling of Passive Water Management in a Miniature Fuel Cell

Journal
ECS Transactions, 92(8)

ISSN
1938-5862

Authors
Chintam, Kavitha
Gerhardt, Michael R
Baker, Andrew M
et al.

Publication Date
2019-07-03

DOI
10.1149/09208.0395ecst

Peer reviewed

Imaging and Modeling of Passive Water Management in a Miniature Fuel Cell

K. Chintam[a], M. R. Gerhardt[b], A. M. Baker[a], D. Richard[a], M. S. Wilson[a], J. Flesner[a], T. Rockward[a], D. S. Hussey[c], J. M. LaManna[c], D. L. Jacobson[c], J. A. Rau[a], A. Z. Weber[b], and R. L. Borup[a]

[a] Los Alamos National Laboratory, Los Alamos, New Mexico 87545, USA
[b] Lawrence Berkeley National Laboratory, Berkeley, CA 94720
[c] National Institute of Standards and Technology, Gaithersburg, MD 20899, USA

A small microwatt fuel cell stack with 8 cells was designed, fabricated, and tested for passive operation with pure H2 and O2 to provide continuous power for multiple decades with uncontrolled fluctuating ambient conditions. The stack was designed to operate with dead ended gas flows with water removal via passive membrane diffusion to notches in the bipolar plates. Two stacks with active areas of 0.2 cm^2, one with 200 µm of membrane and the other with 400 µm, were assembled and tested at varying temperatures and current conditions. Temperatures ranged –55 ºC to 70 ºC, with focus on the lower temperatures. Factors affecting water production and removal included temperature, gas crossover, and membrane thickness. Currents were applied from 16 µA to 10 mA after the cells were stabilized at temperature, followed by a period of drying to observe water transport to the external peripheries of the cell. A two-dimensional multiphysics model was developed to further explore the water management system in varying conditions.

Introduction

Microwatt fuel cell stacks and systems are useful for providing long-term, continuous power to systems that experience a wide range of temperatures and relative humidity (RH) levels. These microwatt fuel cell stacks have advantages over traditional lithium-ion batteries in their potential for applications that require prolonged periods of storage or operation. The continuous discharge and cycling of lithium-ion batteries allows for a maximum lifetime of 10 years (1). This maximum disregards any potential issues with overcharging and limited operation at high and low temperatures (1). Conversely, microwatt fuel cells can have lifetimes of multiple decades when fed with supplies of H2 and O2 in stationary applications (2). Lithium-ion batteries also face fire hazards due to exothermal runaway from

storing high energy densities (3). Microwatt fuel cell systems, however, store the reactants in separate vessels, and thus are not subject to self-discharge or exothermal runaways. Any storage issues that may arise in the operation of a microwatt fuel cell, therefore, will not lead to hazards to the degree of lithium-ion batteries. The service life, wide range of operating conditions, and safety of microwatt fuel cells are advantages over traditional lithium-ion batteries that have attracted interest for low power, long-term power sources.

Microwatt fuel cells are derived from the widely-researched proton exchange membrane fuel cells (PEMFCs), which allows for the benefits of PEMFCs on a much smaller scale. However, this small scale is accompanied by its own set of challenges. In contrast to typical kilowatt-scale fuel cells for transportation applications, microwatt fuel cell stacks encounter system challenges with gas reactant membrane crossover and gasket- leakage, as well as electronic conduction through the membrane, called internal leakage current. In terms of crossover, oxygen permeates at about half the rate of hydrogen, which can significantly affect the voltage at low current densities (4, 5), a phenomenon that is exacerbated at smaller scales. The 2020 U.S. Department of Energy technical target for membrane internal leakage current is an equivalent DC resistance of 1000 Ω*cm^2, which would cause a normal 30 year H2 reactant supply to dwindle down to last less than a year, illustrating the magnitude of the issue with current technology (6). Moreover, consistent supplies of O2 are necessary to avoid dependence on air availability and purity. Since the stack reactants supplied are dead-ended, necessary measures must be taken to prevent the buildup of water to prevent system failure.

In past work, similar assemblies of these microwatt fuel cells and their water management systems were imaged, however, only at temperatures at and above 25 ºC (7). In this work, the passive water management system in the microwatt fuel cell is further studied and shown to be successful at temperatures down to −20 ºC, but requires additional design considerations at freezing and below-freezing temperatures to prevent gas crossover. A two-dimensional multiphysics model to simulate water management was developed to better define the water management requirements. This model is based on a previous model by Zenyuk, *et al.* (8). The model aids in confirmation of observed effects during experimentation, such as crossover and water production at low temperatures. In future developments, it will be used for prediction under varying conditions.

Experimental

Cell Design

The need to maintain space for internal gas manifolds and tubing leads to a 1.3 cm x1.9 cm stack area, with an active area of 0.2 cm^2. The design of the stack is shown in Figure 1.

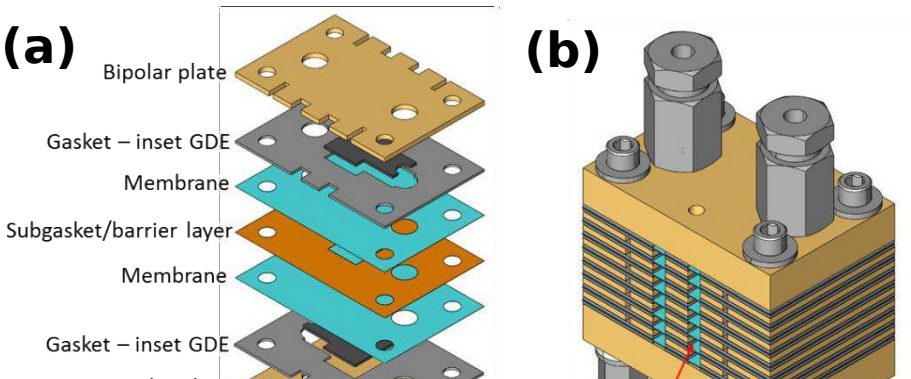

Figure 1. Drawing of (a) stack components of microwatt fuel cell and (b) complete 8-cell stack with water removal notches indicated.

The purpose of the notches in the bipolar design is to accelerate water removal away from the active area and leave exposed membrane for water evaporation, preventing flooding and subsequent failure of the system. Stacks were built and tested with 4 and 16 layers of Nafion XL membrane resulting in 100 µm and 400 µm thicknesses respectively. The catalyst layers contain 4 mgPt*cm-2 with a 1 mg*cm-2 Nafion overcoat. [Certain trade names and company products are mentioned in the text or identified in an illustration in order to adequately specify the experimental procedure and equipment used. In no case does such identification imply recommendation or endorsement by the National Institute of Standards and Technology, nor does it imply that the products are necessarily the best available for the purpose.] The bipolar plates had a thickness of 0.5 mm and the gas diffusion electrodes (GDEs) used were Sigracet 29 BC with a thickness of 235 µm.

Constant compressive forces were maintained by the use of a series of three Belleville washers as in Figure 2 to address stack thermal expansion and contraction.

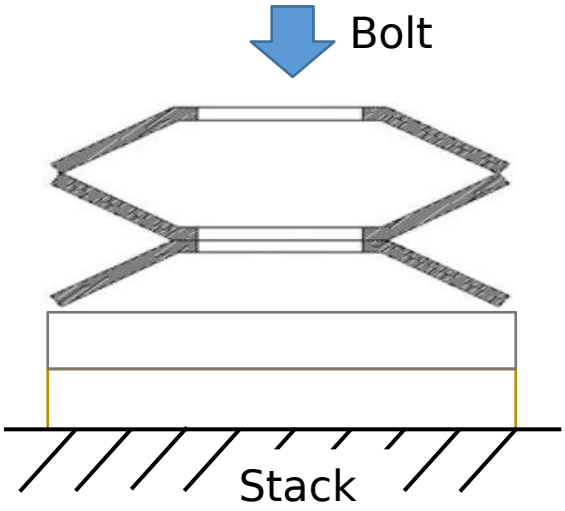

Figure 2. Diagram of Belleville washer usage.

Gas diffusion electrodes with nominal Pt-black areal density of 2 mg*cm^{-2} were used for both the anode and cathode for durable operation. End plates and bipolar plates were fabricated out of titanium. An eight-cell stack was used to provide a minimum of four volts. The gasket was comprised of PTFE for neutron imaging.

Cell Testing and Characterization

HFR. High frequency resistance (HFR) was measured at the desired temperature and RH conditions using galvanostatic electrochemical impedance spectroscopy at either 0 A (OCV) or 16 µA from 1 MHz to 1 Hz with a bias of +/- 1 µA. The real impedance intercept in the Nyquist

plot was taken to be the HFR.

Neutron imaging. In order to track water concentrations at varying conditions, neutron imaging was performed at the National Institute of Standards and Technology (NIST) at the Neutron Imaging Facility on beam tube 2 (BT2) (5). Experiments were performed on

two stacks with Teflon gaskets and different membrane thicknesses: a 200 µm membrane stack and a 400 µm membrane stack.

Gas flow to the stack was dead-ended, while back pressures were controlled by flowing in an external circuit. When gases were turned off, the external circuit and back pressure were turned off, but lines were not evacuated. Hence, gas pressure was reduced to 100 kPa-absolute when gases were turned off, with no ability to re-supply flow. Current was controlled using a Biologic SP-240 potentiostat, and temperatures other than 25 °C were controlled using pad heaters on either side of the cells and a temperature controller. Temperatures below 25 °C were controlled by use of a liquid nitrogen cooled series of insulated boxes, shown in Figure 3, with the external box heated with pad heaters to prevent external water condensation during imaging. All experiments were run with the cells bolted in the box, to allow for consistency of background noise from the box setup in all images.

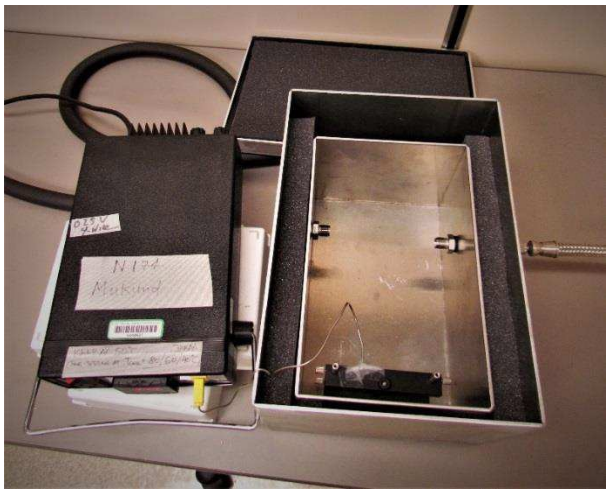

Figure 3. Picture of cooling system for neutron imaging at freezing and below-freezing temperatures.

For all experiments, images were collected every five seconds, for a total of seven seconds per image due to a two second period to write to the data file. The ambient relative humidity in the beam room was between 15% and 20%, but was not monitored. Voltage was also observed to ensure minimal fluctuations. Low resolution mode imaged the whole cell through-plane using a 15 mm diameter aperture with a fluence rate of
1.38×10^{7} $cm^{-2}s^{-1}$ and a Nikon 85mm f/1.8 photo lens with a PK11 extension ring that produced a spatial resolution of about 60 µm. The images were processed by subtracting a “dark” image, followed by dividing the wet images by the dry images and using the log transform of the transmission to calculate the water thickness (mm) in the membrane electrode assembly (MEA) with relation to the center of the membrane. Each pixel is equivalent to 6.5 µm. The water thickness

profiles are averaged in the vertical direction.

In the neutron images, the gas ports, tie bolts and nuts, and inlet gas lines are visible. The active area of 0.2 cm^2 is evident by the high water concentration in the square, with water at a high concentration also visible in the GDE outside the active area where the GDE extends to the gas port for gas transport from the gas inlet to the active area. Figure 4 depicts the relevant areas mentioned.

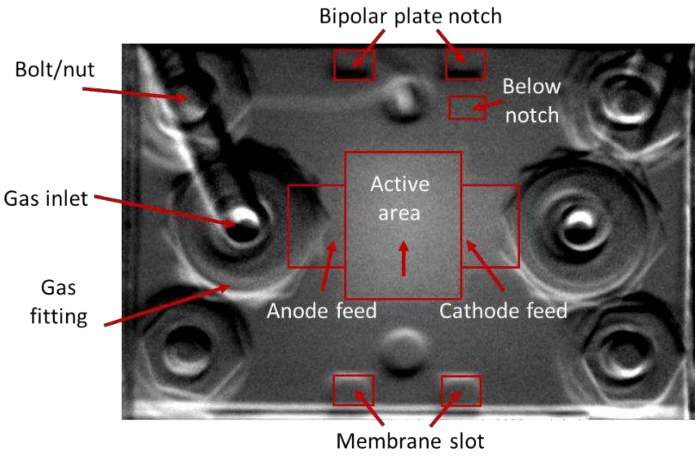

Figure 4. Neutron image of cell with labelled parts.

Modeling. A two-dimensional multiphysics model was developed to help elucidate water transport phenomena and inform a greater cell model. The main differences between this model and our previous work (7) are the model geometry and the inclusion of time- dependent terms in the gas transport, water transport, and heat equations to enable transient simulation. Figure 5 shows the updated model geometry.

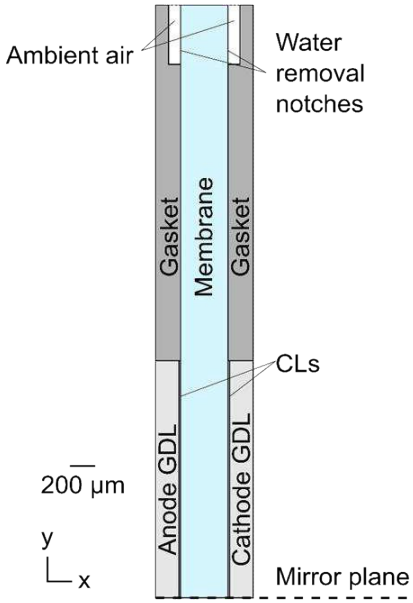

Figure 5. Diagram of water transport model setup with labelled parts.

The model assumes a backpressure of 100 kPa on both the anode and cathode. The gas composition is set to pure hydrogen at the anode and pure oxygen at the anode, humidified to the stated relative humidity. Unless otherwise noted, the model used an external ambient RH of 15% to mimic experimental conditions. The ambient air slots are assumed to contain nitrogen at 15% RH for simplicity. A 0.2 cm^2 active area is used, as in the actual stacks. The membrane thickness is varied depending on the stack being analyzed. The rate of water absorption and desorption from the exposed membrane surface is calculated

based on the difference between gas RH and membrane water activity, a0, as shown in Equation 1:

$$J_{w,des} = k_{des}(a_w - a_0). \quad [1]$$

The value of *kdes*, defined as the rate of desorption, influences whether the membrane can wick away all of the produced water. A reasonable fit between the model and experimental data was found by using a $\square_{des}$ value of 1.0 $\times 10^{-6}$ mol*cm^{-2} s^{-1}, which is about a factor of 5 higher than the value for Nafion according to Kienitz as shown in Equation 2 (9), assuming 15% RH.

$$\square_{des} = 1.04 \times 10^{-7} \exp(4.48\square_0) \text{ mol*cm}^{-2}\text{ s}^{-1}) \qquad [2]$$

Hydrogen crossover through the membrane was calculated using Fick's law:

$$\frac{\square c_{\square_2}}{\square t} = \nabla \cdot \square \nabla \square_2 \square_2 , \qquad [3]$$

where $\square_{\square_2}$ is the permeability of hydrogen in Nafion taken from Schalenbach, *et al.* (10),

$\square_{\square_2}$ represents the partial pressure of hydrogen $= \frac{\square_{\square_2}}{\square\square}$. The partial pressure of gas, and $\square_{\square_2}$ hydrogen gas is set to zero at the anode CL/membrane boundary, as it is assumed all the hydrogen reaching the anode reacts with oxygen to make water.

Results

HFR. High frequency resistance results are shown in Figure 6. Measurements indicate a negative correlation between temperature and HFR. The AsR Ti 400 µm sample is one of the stacks on which neutron images were taken.

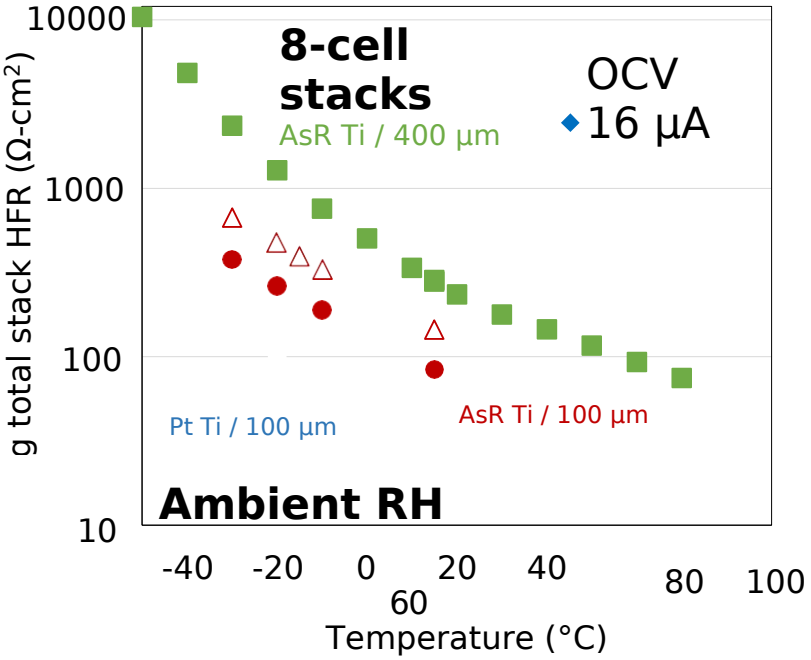

Figure 6. HFR measurements for different samples versus temperature. Measurements are provided for three stacks (i) 400 µm membrane

thickness with titanium plates (green), (ii) 100 µm membrane thickness with titanium plates (red), and (iii) 100 µm membrane thicness with platinum coated titanium plates (blue). Open symbols represent HFR at OCV, filled symbols represent HFR at 16 mA of current.

Neutron imaging. The cell was operated at various temperatures and currents with gases flowing, followed by turning the current off to allow for drying. Although current dictates water production rates, temperature can affect water dissipation rates and, therefore, overall water content at different times. Drying happened as expected for temperatures above
−20 °C. At temperatures at and below −20 °C, water production was greater than the amount of water removal via the passive water management strategy even with the current turned off, rather than a drying of the cell as expected, as shown in the top curve in Figure
7. With the gases turned off and no back pressure, as shown in the bottom curve of Figure 7, drying occurred, indicating that gas crossover happens with the gases on at low temperatures. However, this drying is minimal, likely due to the inability to dry quickly at low temperatures.

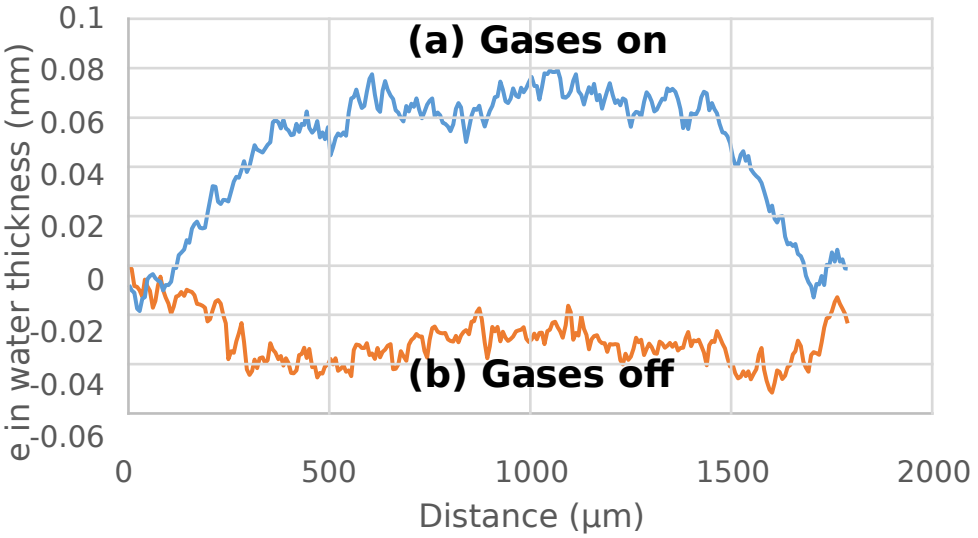

Figure 7. Plot of the change in water thickness in the 400 µm stack active area after two hours of operation at −30 °C with no current and (a) gases on, showing positive water formation due to gas crossover and (b) gases off, indicating drying and water depletion from negative water thickness change.

For the 200 µm stack, current was held at 16 µA for two hours at 0 °C and −20 °C, and one hour at 25 °C. Water formation in the active area and the area below the notch was observed and is shown in Figure 8.

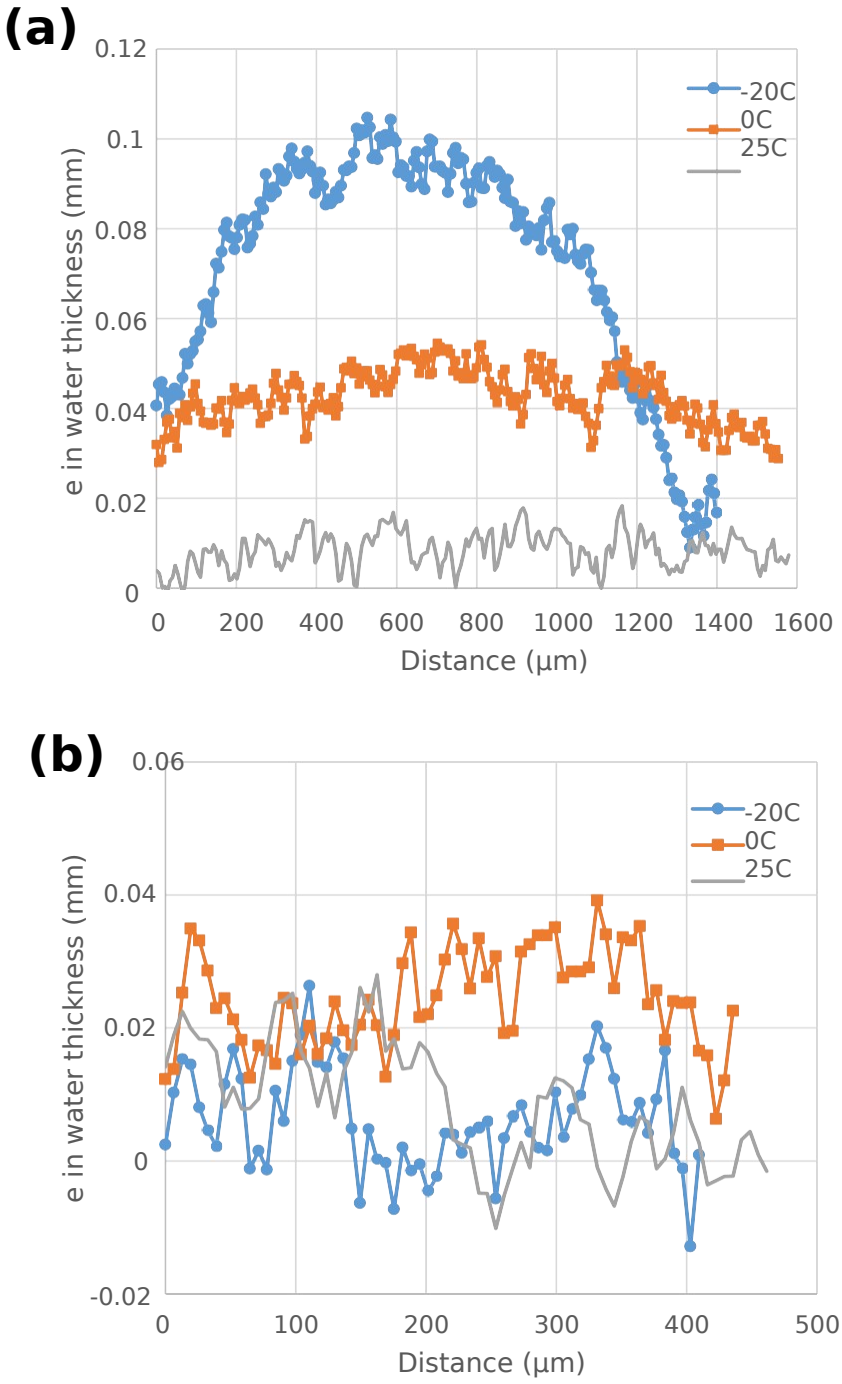

Figure 8. Change in water thickness profiles of the 200 µm stack at 16 µA at three different temperatures after two hours of the (a) active areas and (b) small areas below the water- removal notch.

As shown in Figure 8a, the average increase in water thickness in the active area is inversely related to the temperature. It should be noted, however, that the sequence of wetting went from 25 °C, to 0 °C, to −20 °C, so the change is not as drastic as the graph indicates. Discussion later on compares the step changes of thickness, rather than overall. However, there is still an increase, possibly because of ice buildup on the edge of the membrane, inhibiting water movement out of the cell. Figure 8b indicates that there is no clear correlation between temperature and water formation below the notch. This is likely because the water formation occurs in the active area, leading to little to no movement of water in surrounding areas. Figure 9 shows the active area difference in water profiles after two hours for the 400 µm stack at −55 °C and 16 µA.

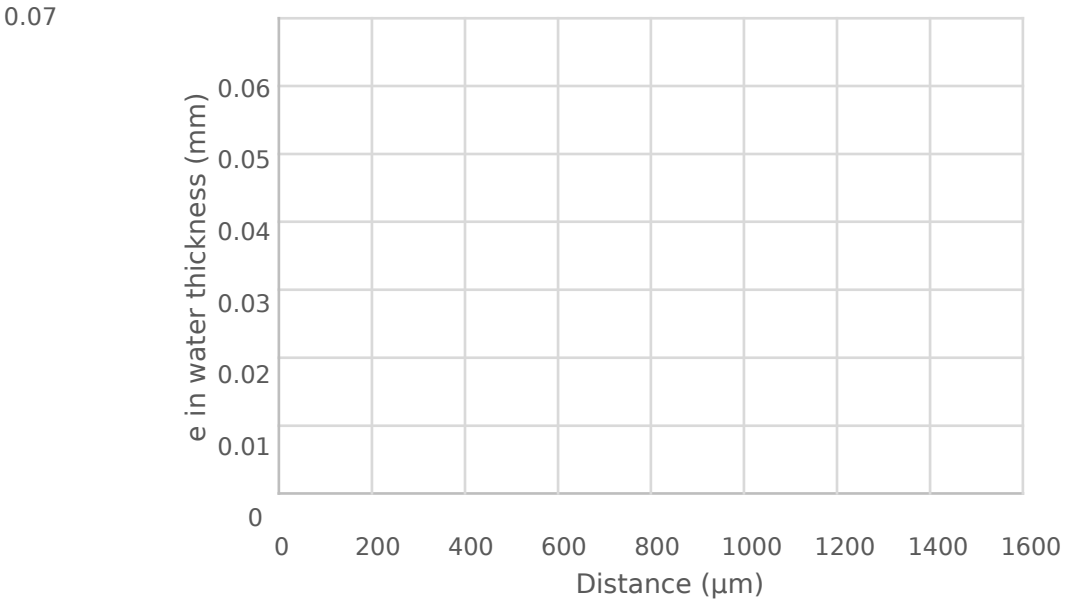

Figure 9. Change in water thickness in active area of 400 µm stack after two hours of wetting at 16 µA at −55 °C.

Figure 9 depicts a likely reduction in crossover and wetting of a completely dry membrane, explaining why it appears to show less water formation than the −20 °C profile in Figure 8. In fact, the average change in water thickness at −55 °C for the 400 µm stack is 0.040 mm, while it is 0.073 for the 200 µm stack at −20 °C. Subtracting out the initial water thickness at 0 °C, 0.043 mm, the step change in water thickness for the latter is
1.30 mm. Based solely on membrane thickness, the 400 µm stack would be expected to hold twice as much water as the 200 µm stack, since there is two times the amount of membrane to keep water in. However, at a constant current, generation is equivalent. The primary reason for difference in water thickness here is crossover. Crossover is twice as fast in the 200 µm stack since the membrane is half as thick as the 400 µm stack. Since there is not a linear trend in water thickness in Figure 8, it is difficult to extrapolate what the water thickness would be at −55 °C. Based on the aforementioned factors,

however, it is reasonable that the 200 μm at −20 °C has more water than the 400 μm at −55 °C.

Membrane A (moles water per mole sulfonic acid sites) are calculated using the following equation:

$$\lambda = \frac{t_w}{L + t_w} * \frac{V_m}{V_w} + \lambda_{dry} \quad [4]$$

where *tw* is the water thickness from the imaging, *L* is the dry membrane thickness of the stack (200 µm or 400 µm), *Vm* is the partial molar volume of the dry membrane (550 cm3*mol-1), *Vw* is the partial molar volume of water (18 cm3mol-1). λ_{dry} is the A of the dry membrane, which is approximated to be 2.3 based on a previous work by Spernjak, *et al*. (11). The total thickness in the *z* direction must be used to account for the variation in swelling from water. This is a departure from the more commonly used equation for through-plane imaging, where only the *x* direction length is used, as in Hussey, *et al.* (12). Figure 10 displays each neutron image and step, while Figure 11 shows the change in water A for the 400 µm stack with changes in temperature and current.

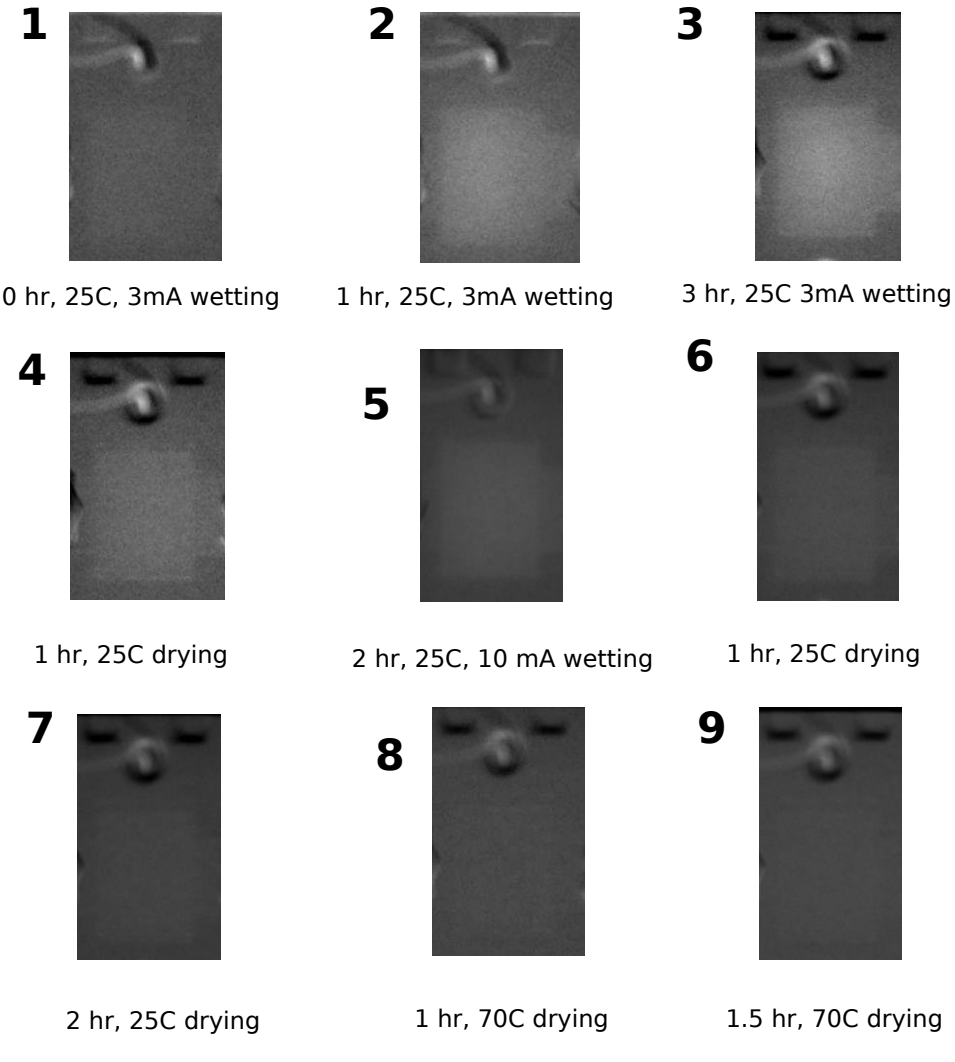

Figure 10. Sequence of images with corresponding number of hours into each step, temperature, and current. These are cropped images of the whole cell as shown in Figure 4 to focus on the active area and the area below the notch as indicated in image #1. All drying steps have no current, but gases remain on. White indicates water. Note that the last two images (#8, #9) in the set are scaled differently in contrast than the others.

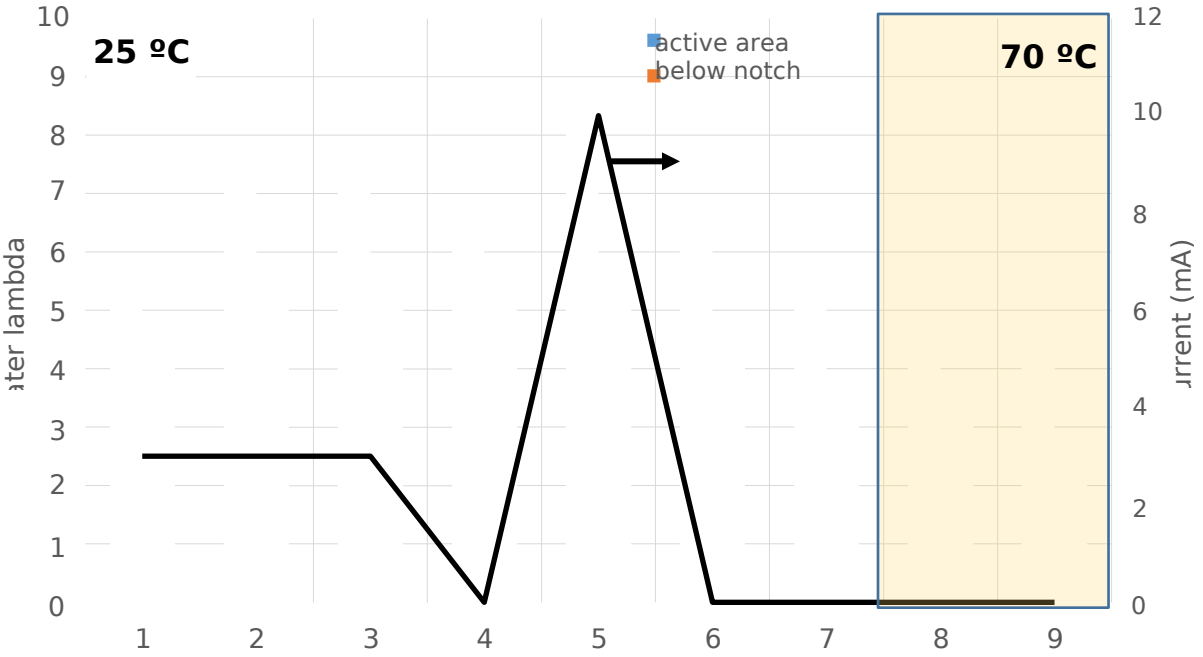

Figure 11. Plot of water A and applied current versus each step corresponding to Figure 10 at varying currents and temperatures. The black line represents the current production during the measurement.

Modeling. To validate the model, the same conditions were simulated as those of the neutron imaging experiments. Figure 12 shows a comparison between modeled and observed water thickness profiles at 25 °C and 3 mA. The rate of water desorption from the ionomer and membrane was used as a fitting parameter as described earlier. The discontinuities in the model curves mark the edges of the catalyst layer, at which an ionomer with some water content is replaced by a dry gasket material. The model reproduces the general shape of the water distribution and its increase over time.

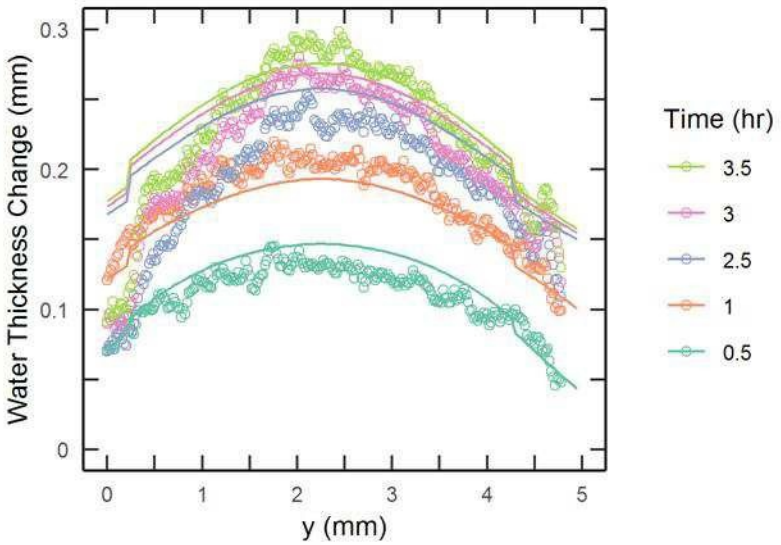

Figure 12. Simulated (lines) and measured (open circles) changes in

water thickness profiles over time at 25 °C and 3 mA.

Further modeling was performed to explore water management in similar systems. Figure 13 depicts water content changes at 25 °C and −55 ° C during a current of 16 μA in a 400 μm membrane stack. It should be noted that the water A values here were calculated in a different manner than in the experimental results (Figure 11). For experimental results, Equation 4 was used to incorporate the water thickness gleaned from neutron imaging results. For the model, A is calculated using water activity as described in Ref. (8).

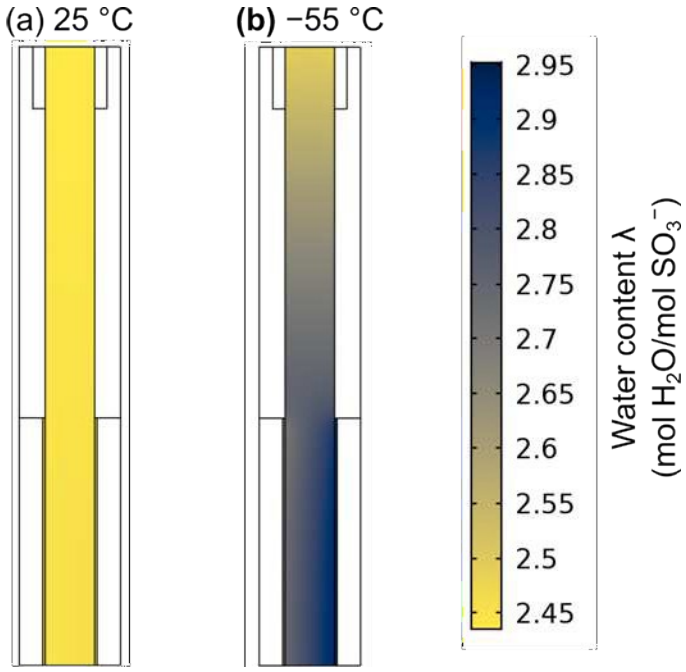

Figure 13. Plots of water content changes described by model at 16 μA at (a) 25 °C and (b)
−55 °C.

Figure 13a illustrates that at room temperature, water transport is fast enough that water content is essentially uniform. However, Figure 13b shows that at −55 °C, water content does change appreciably, and a larger water concentration gradient is necessary to drive water flux out towards the notches. This latter phenomenon was observed in the experiments, as water was not easily transported away at temperatures below −20 °C.

Figure 14 shows how at low temperatures, the water gradient across the membrane takes time to develop. For short time intervals, there is a rapid increase in water content in the cathode catalyst layer, whereas the water content gradient develops through the membrane slowly for long time intervals, indicating that over 4 hours of operation time is required to reach steady-state water content distribution.

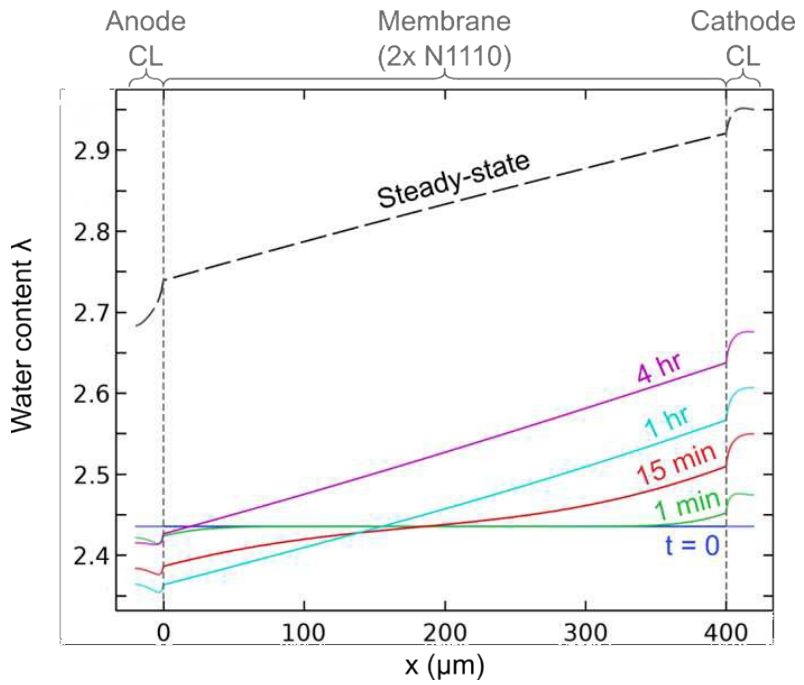

Figure 14. Development of through-plane water content profile over time at −55 °C in a stack with 400 μm of membrane.

Another feature of the model is the ability to estimate crossover current density. Initial crossover modeling indicates that there is higher crossover at higher temperatures, as shown in Figure 15. This calculation qualitatively agrees with the experimental measurements showing little water production due to gas crossover at −55 °C (Figure 9). These results also quantify the reduction in hydrogen crossover expected from using thicker membranes.

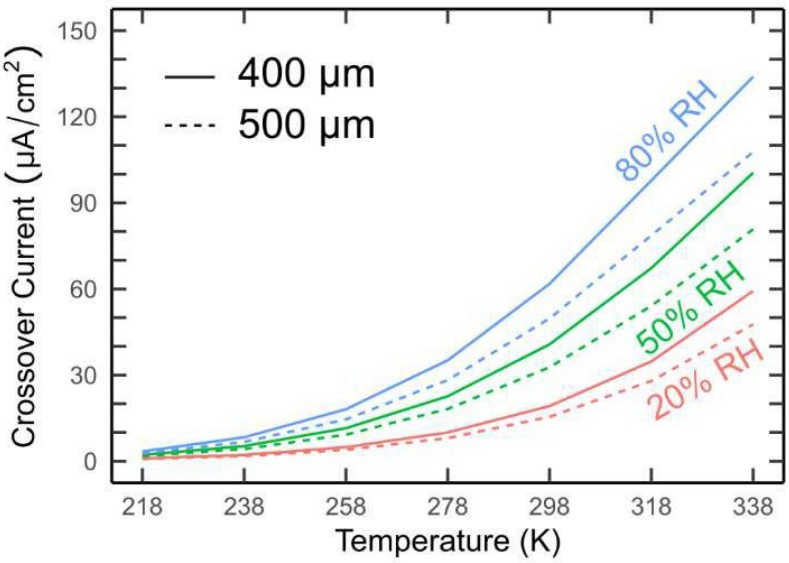

Figure 15. Plot of initial crossover modeling results at varying temperatures, relative humidity levels, and membrane thicknesses, based on a steady-state model applied at 16 μA.

Conclusions

A microwatt fuel cell was designed to operate on H2/O2 with passive operation and water transport. Two stacks of membrane thicknesses of 400 µm and 200 µm were designed and manufactured to assess the passive water management system via neutron imaging. The stacks were exposed to temperatures ranging from −55 °C to 70 °C while neutron imaging was taking place, allowing water production and depletion to be observed at varying currents. Factors affecting water production and removal include temperature, gas crossover, and membrane thickness. At temperatures below −20 °C, gas crossover was more prominent, as water stayed constant or increased even with current turned off. When gases were also turned off, water started depleting, indicating that gas crossover was indeed the cause. Water A values were also calculated to quantify the water movement. A two dimensional multiphysics model was constructed to delve deeper into water management in the system. Water content trends at room temperature and below freezing temperatures were similar to those seen in experiments. Crossover also agreed with low temperature results, indicating a positive correlation between temperature and crossover, explaining why production was low at below freezing temperatures. Additional development of the model will provide valuable insight into microwatt fuel cells in general, a valuable technology for real-world applications.

Acknowledgements

This work was supported by the U.S. Department of Energy. Los Alamos National Laboratory, an affirmative action equal opportunity employer, is managed by Triad National Security, LLC for the U.S. Department of Energy's NNSA, under contract 89233218CNA000001.

References

1. V. Marano, *et al.*, 2009 IEEE Vehicle Power and Propulsion Conference, p. 536-543 (2009).
2. *Multi-Year Research, Development, and Demonstration Plan*, U.S. Department of Energy, 3.4, p. 27 (2016).
3. C. Mikolajczak, M. Kahn, K. White, and R. T. Long, The Fire Protection Research Foundation, Massachusetts, p. 15 (2011).
4. S. S. Kocha, J. D. Yang, and J. S. Yi, *AIChE Journ.*, 52 (5) 1916-1925 (2006).
5. T. Sakai, H. Takenaka, N. Wakabayashi, Y. Kawami, and E. Torikai, *J. Electrochem. Soc.*, 132 (6) 1328-1332 (1985).
6. *DOE Technical Targets for Polymer Electrolyte Membrane Fuel Cell Components*, U.S. Department of Energy (2016).
7. K. Chintam, M. S. Wilson, T. Rockward, S. Stariha, A. M. Baker, E. L. Brosha, D. S. Hussey, J. M. LaManna, D. L. Jacobson, J. A. Rau, and R. L. Borup, "Microwatt Fuel Cell for Long-Term and Wide Ambient Temperature Range Operation". ECS Transactions, 86 (13): 233-244 (2018).

8. I. V. Zenyuk, P. K. Das, and A. Z. Weber, *J. Electrochem. Soc.*, 163, F691– F703 (2016).
9. B. Kientiz, H. Yamada, N. Nonoyama, and A. Z. Weber, J. Fuel Cell Sci. Technol. 8, 011013 (2011).
10. M. Schalenbach, T. Hoefner, P. Paciok, M. Carmo, W. Lueke, and D. Stolten,

J. Phys. Chem. C, 119, 25145–25155 (2015).
11. D. Sperkjak, P. P. Mukherjee, R. Mukundan, J. Davey, D. S. Hussey, D. L. Jacobson, “Measurement of Water Content in Polymer Electrolyte Membranes Using High Resolution Neutron Imaging”. ECS Transactions, 33 (1): 1451- 1456 (2010).
12. D. S. Hussey, D. L. Jacobson, M. Arif, K. J. Coakley, D. F. Vecchia, *J. of Fuel Cell Science and Tech.*, 7, 021024 (2010).